energies

Article

Energy Saving Thermal Management of Space Remote Sensor and Validation

Pan Lu [1,2,*], Teng Gao [1,2], Quanwang Chen [3] and Xiaohan Ren [4,*]

[1] Beijing Institute of Space Mechanics and Electricity, Beijing 100094, China
[2] Key Laboratory for Advanced Optical Remote Sensing Technology of Beijing, Beijing 100094, China
[3] Shandong Institute for Product Quality Inspection, Jinan 250102, China
[4] Institute of Thermal Science and Technology, Shandong University, Jinan 250061, China
* Correspondence: mylifelp@163.com (P.L.); renxh@sdu.edu.cn (X.R.)

Abstract: An energy-efficient thermal control management method for space remote sensors using optical, mechanical, electrical, and thermal integration is proposed. The satellite power resources are insufficient, so an energy-efficient loop heat pipe (LHP) is designed for six intermittently operating detectors. The charge-coupled device (CCD) has a total heat generation of 72 W and operates for 8 min per orbital cycle. The LHP includes a capillary pump, six cold plates, and two radiators. The working fluid of the LHP is high-purity ammonia and the material of the wick is ceramic. The drive power on the capillary pump evaporator automatically switches between 30 W and 90 W depending on the operating mode of the remote sensor, resulting in an average power saving of about 58.2% compared to a conventional LHP. For the optical structure, a three-stage insulation technology was developed to save heater power and improve temperature stability. A transient numerical simulation model of the LHP was developed to study the vapor–liquid zone of two radiators under the condition of rapid power change. Vacuum thermal tests were conducted and the test data agreed well with the numerical simulation results. The in-orbit temperature data showed that the temperature fluctuations of the optical structure and CCD were less than ±0.2 °C and ±0.8 °C, respectively.

Keywords: thermal design; loop heat pipe; remote sensor thermal control

check for updates

Citation: Lu, P.; Gao, T.; Chen, Q.; Ren, X. Energy Saving Thermal Management of Space Remote Sensor and Validation. *Energies* **2023**, *16*, 864. https://doi.org/10.3390/en16020864

Academic Editor: Jian Liu

Received: 17 December 2022
Revised: 31 December 2022
Accepted: 2 January 2023
Published: 12 January 2023

1. Introduction

With the development of remote sensing technology, one of the most important technical innovations is the application of a charge-coupled device (CCD) in the spacecraft. The remote sensor has stepped into the era of continuously working data transmission satellite, and it is necessary to thermally control the CCD and focal plane assembly [1,2]. The CCD of some satellites can realize the temperature index in a passive way. The external ultraviolet imaging telescope (EIT) is a high-resolution, wide-field, multi-band RC telescope, the thermal range of the optical structure is 19.5 °C~20.5 °C during its operational life, and the CCD is conductively connected to an external radiator, cooling the detector down to −80 °C [3]. PLEIADES high-resolution optical satellite requires a gradient between CCDs lower than 1 °C and an increase in the detector temperature of less than 4 °C peak-to-peak during imaging time, and the total dissipation of 10 CCD detectors is 4 W. The power dissipated by the detectors and by the front-end electronics is evacuated by conduction through the main structure towards three copper braids that link the structure to a heat pipe [4]. Li et al. [5] studied two copper thermal straps used in the thermal control of CCD, of which the power consumption is 0.446 W; in long-term operation, the temperature fluctuation of the CCD varies from −69.3 °C~−62.2 °C and the temperature range of optical lens is −7 °C~−3 °C. LHP is gradually applied to the thermal control of CCD; Choi [6] designed 2 LHPs and 12 heat pipes for 256 detectors, of which the power consumption is 0.58 W, the temperature change of 256 detectors is 1 °C, the CCDs work in long-term mode, so the vapor–liquid phase zone is basically unchanged. Khrustalev et al. [7] developed a transient model of two strongly thermally coupled LHPs on the Thermal Desktop™ platform, but the vapor–liquid phase zone was not analyzed. Given the lack of support from on-orbit data, the accuracy and effectiveness of existing models have not been verified.

This space remote sensor sets a strict temperature range and stability index; however, if the satellite is short of power, the conventional thermal control design cannot meet the power requirements provided by the satellite. Therefore, a low power consumption thermal management is needed. For the optical system, three-stage heat insulation technology is designed to minimize the heat leak from the lens to space. An energy-saving LHP is designed for high power CCD in short-term operation mode, the driving power on LHP varies according to the working mode of CCD, the unfavorable result is the drastic change in the vapor–liquid phase zone in radiators. After detailed design, the thermal management of optical structure and CCDs experienced extremely thermal environment assessment on-orbit, and all the temperature indicators show that the thermal control system completely meets the requirements.

2. Remote Sensor Composition and Thermal Control Index

The remote sensor is mounted in the main frame, which is a box-type load-bearing structure composed of carbon fiber skin and an aluminum honeycomb sandwich structure, has the characteristics of high strength, light weight, and small thermal deformation, and fixes the remote sensor precisely. The remote sensor is composed of off-axis three-mirror reflective lenses and a linear CCD focal plane assembly (FPA). The mirrors of the lens are glass-ceramics with low coefficients of thermal expansion, are lightweight, and the structure of the lens is M40J carbon fiber material. The FPA includes six CCDs, six circuit boxes, a base, and two focusing mechanisms mounted at both ends of the FPA base; when the focusing mechanisms are working, the FPA could generate ±4.5 mm displacement. Outside the main frame is a truss, made of carbon fiber. The size of the remote sensor is 3.5 m (length) × 2 m (wide) × 3.5 m (height), as shown in Figure 1.

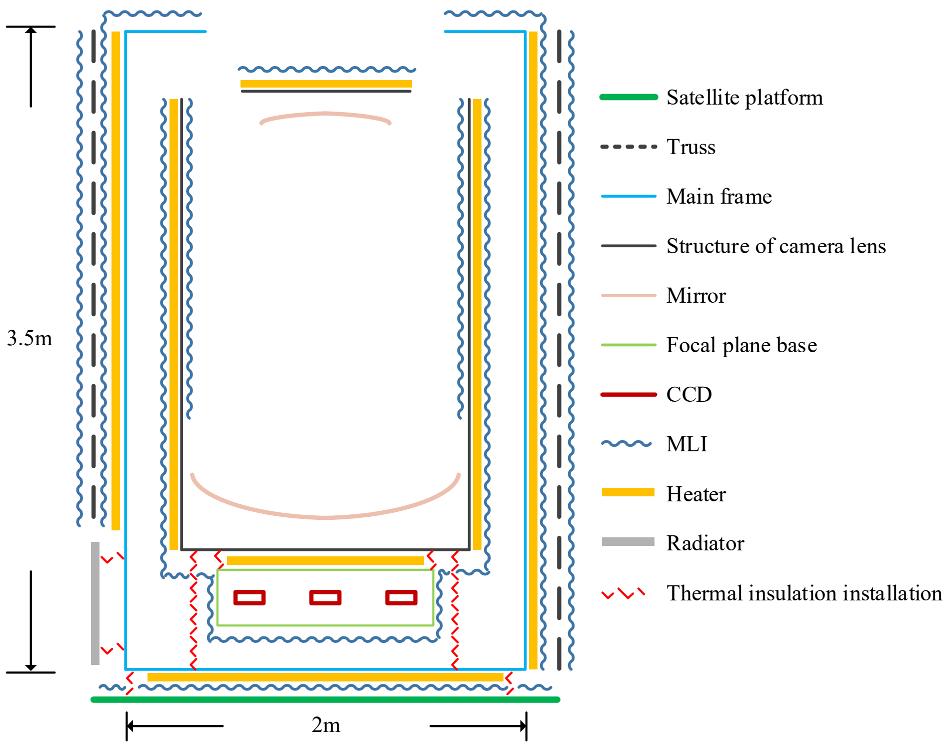

Figure 1. Schematic of the space remote sensor.

The working mode and heat generation are shown in Table 1; the period of the orbit is about 95 min. The thermal control index is shown in Table 2.

Table 1. Heat consumption and operating time of remote sensor heat source.

Assembly	Heat Generation of Each One/W	Working Mode/(min·orbit^{-1})
CCD	12	8
FPA circuit	21	8

Table 2. Temperature control requirements of remote sensor key components.

Assembly	Temperature Range/°C	Long Term Temperature Fluctuation/°C
Main frame	10~22	±0.5
Lens-mirror	18~22	±0.25
Lens-structure	18~22	±0.25
CCDs	17~23	-

3. Thermal Control Management

Thermal control management makes full and rational use of the satellite power supply and is designed for thermal control through a combination of active and passive thermal control measures. The remote sensor is mounted outside the satellite platform and is directly exposed to the harsh space environment, heated by external heat fluxes, i.e., direct solar radiation, Earth albedo, and Earth infrared, while being cooled by the 4 K background. The satellite has ±32° roll, ±26° pitch, and ±90° yaw attitude control capabilities, which further complicates the external heat fluxes to the remote sensing system and poses a significant challenge for precise temperature control. Based on the calculation of the angle (β angle) between direct solar radiation and orbit, the +Y direction of the remote sensor is the most suitable radiator direction when the remote sensor is in the normal flight attitude without solar heat flux. The -Y direction of the remote sensor is exposed to solar heat flux in sunlight for a long time; the entrance direction of the Earth remote sensor is +Z, and its external heat flux is stable. In order to cover the worst in-orbit conditions, extreme thermal design conditions considering different dates, normal and maneuvering attitudes, thermal performance degradation of coatings, and temperature variations at the satellite platform interface are analyzed and summarized.

The main frame is the main load-bearing structure, and temperature fluctuations directly reduce the temperature stability of remote sensors and distort the lens. A thermal designed truss surrounds the main frame, and both the outer surface of the truss and the main frame were covered with 15 layers of multi-layer insulation (MLI), except for the radiators zone, and five heaters were set in the ±X, ±Y and, –Z plane of the main frame, where the temperature threshold was [15.8 °C, 16.2 °C] and the total heat power is 35.8 W. The inner surface of the main frame was coated with high emissivity black paint to indirectly control the temperature of the internal optical structure. This method has been shown to achieve more stable temperature variation. The entrance of the remote sensor faces complex and variable external heat flux, and so to guarantee the temperature stability, the inner and outer face of the structure of lens were covered with 15 MLI, of which the color of the outermost surface is black, for the purpose of eliminating stray light. To further suppress the temperature fluctuation of the mirrors, 10 heaters were set on the lens structure, total heat power was 28.3 W, the temperature threshold was [19.8 °C, 20.2 °C]. The lens was mounted on the main frame with a titanium alloy spherical hinge, which unloads the stress and creates a big thermal contact resistance between the lens and the main frame, to further guarantee the temperature stability of the lens. The MLI of the truss, main frame, and the structure of lens formed three-stage heat insulation for mirrors.

The conventional method of axially grooved heat pipe and copper thermal strap is adopted for circuit boxes, but it is not suitable for CCD, since the CCD has the character of low heat capacity, high heat consumption, large number, and compact layout, the distance between CCD and circuit box is only 3 mm, and the heat transfer capacity of a properly sized axially grooved heat pipe is insufficient; at the same time, the big thermal resistance of the copper thermal strap causes a rapid temperature rise in CCD, which exceeds the temperature fluctuation index. LHP is an advanced two-phase heat transfer technology that is the baseline thermal management system for NASA's GLAS, ESA's ATLID, and several other satellites [8,9]. A porous capillary wick is mounted in the evaporator of LHP, the capillary force pumps the working fluid in a closed loop, and when the working fluid undergoes a phase change, a large amount of heat is transferred efficiently. Compared with the grooved heat pipe, the LHP has a larger heat transfer capacity, higher temperature control precision, and better flexibility in the pipe [10,11]. As shown in Figure 2, the LHP schematic mainly comprises the capillary pump assembly, radiator assembly, cold plate assembly, and pipes. The capillary pump assembly consists of an evaporator, a compensate chamber (CC), and a capillary wick, which is in the middle of the pump. The wick is porous, and the diameter of the pore in the wick determines the maximum pressure rise; this is the most important component in the LHP. When the driving heater on the evaporator is switched on, the liquid working fluid turns to vapor and flows into the primary radiator along the pipe, the radiator is then coated with low solar absorbance ratio/high emission white paint. The vapor working fluid releases heat and turns into sub-cooled liquid before flowing into the pre-heater, the sub-cooled working fluid then exchanges heat with the vapor and exits from the evaporator to raise the temperature of the sub-cooled working fluid. Then, the working medium flows into the pre-heater, the heater on the pre-heater turns the sub-cooled liquid working fluid into the vapor–liquid phase, and stays at a low quality. The working fluid flows from the first to the last CCD cold plate to continuously absorb the heat dissipated from the CCDs, to prevent the heat accumulating in CCDs and depress the temperature rise, and the quality of the working fluid keeps rising but the working fluid is still in a saturation state. After that, the working fluid flow into the secondary radiator turns to liquid, pumped by the capillary force from the wick, the LHP cycles continuously. The thermal network diagram of the loop heat pipe model is shown in Figure 3. The purpose of the heater on CC is to precisely control the temperature of the CCD cold plates, since the working fluid in the evaporator, CC, and cold plates is in a saturation state at the same time. There is a thermodynamics correlation,

$$P_{\mathrm{e}} - P_{cc} = \Delta P_{tot} - \Delta P_{w} = \Delta P_{loop} = \frac{dP}{dT}(T_e - T_{cc}) \tag{1}$$

The Clausius–Clapeyron equation:

$$\frac{dP}{dT} = \frac{\lambda}{T_{cc}\Delta v} \tag{2}$$

where P_{e} is the working fluid pressure in the evaporator, P_{cc} is the working fluid pressure in CC, ΔP_{tot} is the total pressure drop in the loop, ΔP_w is the flow resistance of working fluid in the wick, ΔP_{loop} is the flow resistance in external loop, $\frac{dP}{dT}$ is the slope of phase balance of the working fluid, Δv is the difference in specific volume between vapor and liquid working fluid at the temperature of CC, λ is the working fluid latent heat of vaporization.

Most of the heat loaded on the evaporator is used to vaporize the liquid working fluid, the rest is conducted from the evaporator to CC by the capillary wick (back conduction); this part of heat and the heater power on the CC turns the sub-cooled working fluid to saturation state, which can be visualized by the energy conservation formula as shown below:

$$Q_e = Q_{e,cc} + Q_{e,vap} \tag{3}$$

$$Q_{e,vap} = m\,\lambda \tag{4}$$

$$Q_{e,cc} = G_{e,cc}(T_e - T_{cc}) \tag{5}$$

$$Q_{cc} + Q_{e,cc} = C_p \times m \times (T_{cc} - T_1) \tag{6}$$

Q_e is the heat power applied on the evaporator, $Q_{e,cc}$ is the back conduction, $Q_{e,vap}$ is the heat used to vaporize the working fluid in the evaporator, m is the mass flow in the LHP,

$G_{e,cc}$ is the thermal conductivity between the evaporator and the CC, T_e is the temperature of the evaporator, T_{cc} is the temperature of the CC, Q_{cc} is the heat applied on the CC, C_p is the isobaric heat capacity, T_1 is the temperature of working fluid return to CC.

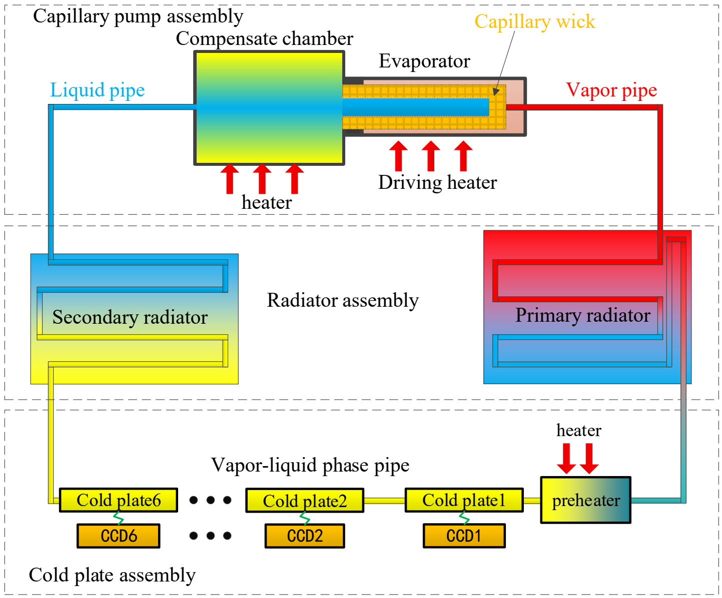

Figure 2. The component schematic diagram of the loop heat pipe.

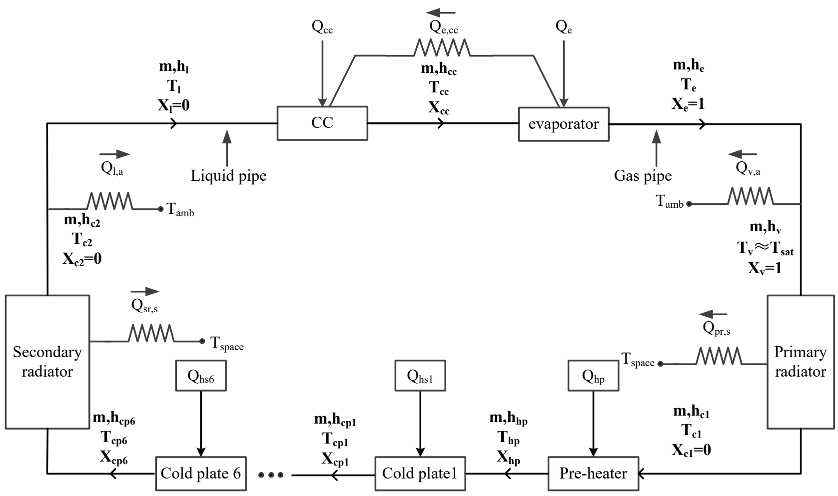

Figure 3. Thermal network diagram of the loop heat pipe model.

There is energy conservation of primary and secondary radiator:

$$\varepsilon\sigma A_{c1}\overline{T}^4_{C1} - Q_{hf1} = Q_{e,vap} + C_p \times m(T_{CC} - T_{C1}) \tag{7}$$

$$\varepsilon\sigma A_{c2}\overline{T}^4_{C2} - Q_{hf2} = Q_{\mathrm{hp}} + Q_{\mathrm{hs}} + C_p \times m(T_{C1} - T_{C2}) \tag{8}$$

where ε is the emissivity of the thermal coating on the radiator, σ is Stephen Boltzmann constant, A_{c1} is the area of the primary radiator, A_{c2} is the area of the secondary radiator, $\overline{T}_{C1}$ is the average temperature of the primary radiator, $\overline{T}_{C2}$ is the average temperature of the secondary radiator, Q_{hf1} is the external heat flux absorbed by the primary radiator, Q_{hf2} is the external heat flux absorbed by the secondary radiator, Q_{hp} is the heater loaded on the preheater, Q_{hs} is the total heat generated of all CCDs, T_{C1} is the temperature in the primary radiator outlet, T_{C2} is the temperature in the secondary radiator outlet.

By the above equations, the heat loaded on the evaporator, CC, and the pre-heater, and the primary/secondary area can be determined, is shown in Table 3.

Table 3. Design parameter of LHP.

Design Items	Parameter
Material of evaporator and reservoir shell and loop	Stainless steel
Outer diameter of evaporator/mm	19
Outer diameter of reservoir/mm	36
Material of capillary core	Ceramic
Average aperture of capillary core/µm	0.5
Porosity of capillary core	70%
Internal diameter of vapor loop and length/mm	2 and 520
Internal diameter of Condense loop in primary radiator and length/mm	2 and 3850
Internal diameter of Condense loop in secondary radiator and length/mm	2 and 2900
Internal diameter of liquid loop and length/mm	2 and 485
Material of radiator	Aluminum alloy
Kind of working fluid	High purity ammonia
Area of primary radiator/m^2	0.38
Area of secondary radiator/m^2	0.32
Power on CC and on pre-heater/W	3 and 5
ε	0.87

To ensure the stable operation of the LHP, the heat used to vaporize the working fluid in the evaporator must be greater than the heat loaded on the cold plate assembly to make the working fluid to undergo a phase change:

$$Q_e - Q_{e,cc} > Q_{hs} + Q_{hc} - C_p \times m(T_{cc} - T_{C1}) \tag{9}$$

The CCDs operate for 8 min every orbit period cycle while generating significant heat, the other 87 min of the orbit they are turned off. The startup of LHP is a time-consuming process, and disadvantageous for the space remote sensor flexible imaging. When the CCD is in standby, a low drive power (30 W) is designed to keep the LHP running, and switch to a higher drive power (90 W), from 3 min before the CCD starts working until 1 min after the CCD stops working, which is an energy-saving method compared to the conventional LHP, whose drive power is constant [10]. This method decreases the periodic average heat consumption by about 58.2%, and the area and mass of the primary radiator decrease by about 60%. The huge variation in power on the evaporator and CCDs makes the working fluid flow unstable, disadvantageous for temperature stability of CCDs, and the vapor–liquid phase zone in radiators change drastically. The NASA-standard thermohydraulic analyzer, Thermal Desktop^{TM} (SINDA/FLUINT), has been used to model various aspects of the LHP operation [12–16]. A transient numerical simulation model was developed on the platform of Thermal Desktop in 0 g to simulate the on-orbit condition. The conduction between the LHP radiators and the main frame, the convection inner the pipe, and the radiation between the radiators to the space, including the external heat flux from the space was solved simultaneously. In the hot simulation case, the radiators absorb the highest external heat flux (maximum β angle), the CCDs work periodically, and the driving power on the evaporator switches between 30 W and 90 W. In the cold simulation case, the radiators absorb the lowest external heat flux (minimum β angle), the CCDs are always on standby, and the driving power on the evaporator is maintained at 30 W. The heater on the CC keeps the vapor–liquid phase of the working fluid in the CC at the temperature of 20 °C ± 0.5 °C in both cases.

Shown in Figure 4 is the temperature of the radiators. The capillary pump is mounted on the secondary radiator, the arrows are the flow direction of the working fluid. Temperature in the hot case is higher than the cold case, and the temperature is not uniform in each radiator; temperature gradually decreases along the pipe. A radiator temperature of about 20 °C means that the working fluid is in vapor–liquid saturation state.

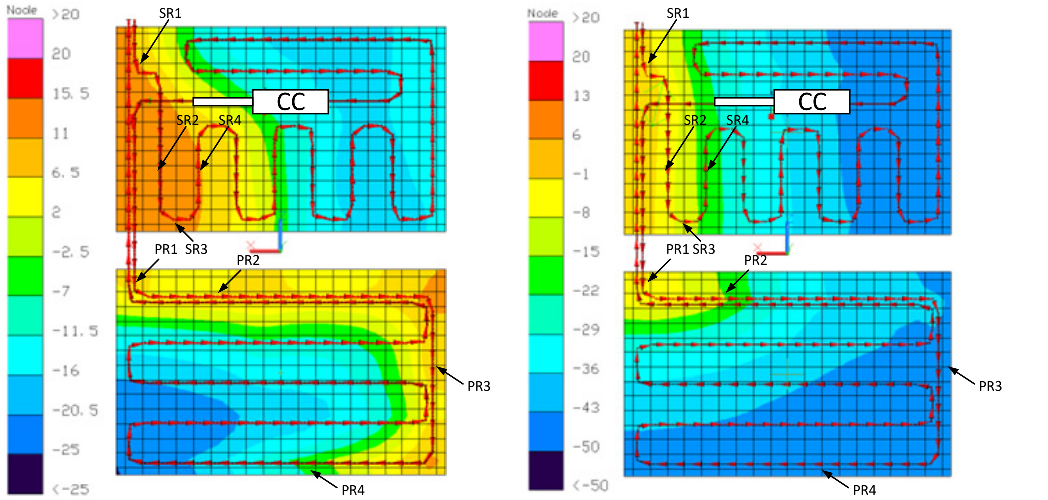

Figure 4. Temperature of the radiators and pipes in simulation (**up**: secondary radiator, **down**: primary radiator, **left**: hot case, **right**: cold case).

Shown in Figure 5 is the quality of the working fluid. In the hot case, the quality of the working fluid decreases sharply from 0.26 to 0.05, because the driving power on the evaporator switches from 30 W to 90 W 3 min before the CCDs start working, and the mass flow of the working fluid increases suddenly. When the CCDs start working, the quality in each cold plate increases until the CCDs stop working, the maximum quality is about 0.43; after that, the quality starts to decrease, and 1 min later the driving power on the evaporator switches from 90 W to 30 W and the quality recovers to 0.3. In the cold case, the quality of the working fluid is about 0.19 in each cold plate.

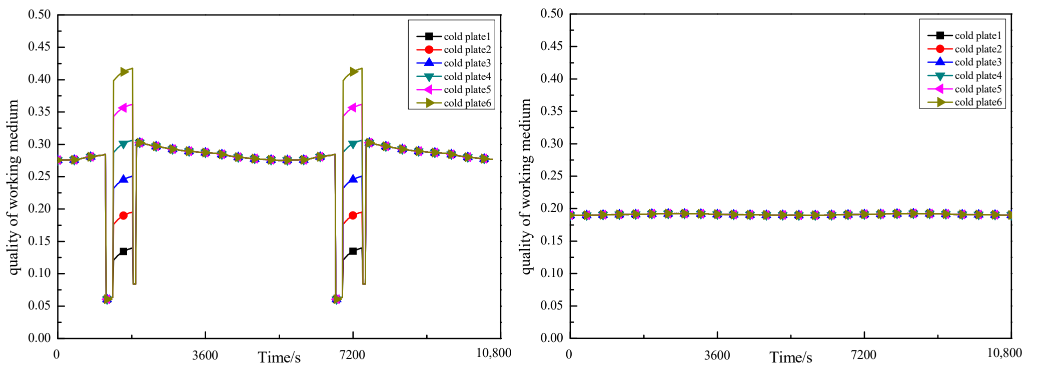

Figure 5. Quality of working fluid in six CCD cold plates in simulation (**left**: hot case, **right**: cold case).

As shown in Figures 6 and 7, the PR1-4 and SR1-4 are the thermocouple positions along the pipe in the primary radiator and secondary radiator. In the hot case, the vapor–liquid phase zone changes with the external heat flux from space, the CCDs' power, and the driving power at the same time. The length variation of the vapor–liquid phase zone in the primary radiator and secondary radiator is about 1 m and 0.93 m, respectively. In the cold case, the vapor–liquid phase zone is stable.

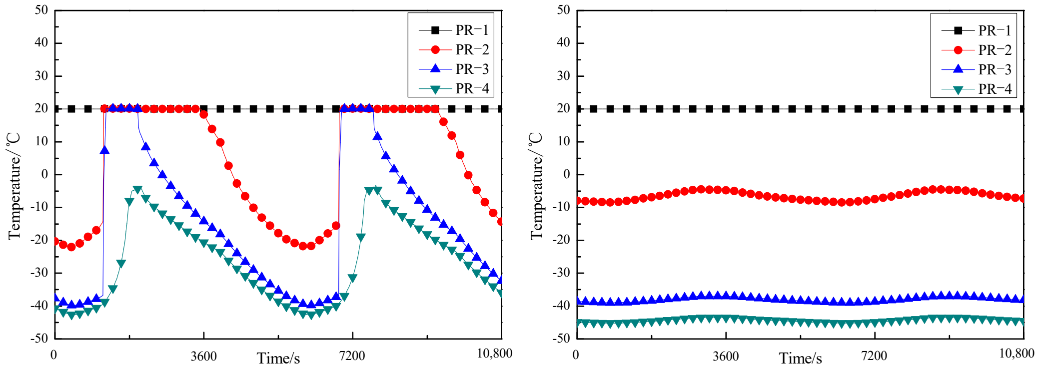

Figure 6. Temperature of the pipes on the primary radiator vs. time diagram in simulation (**left**: hot case, **right**: cold case).

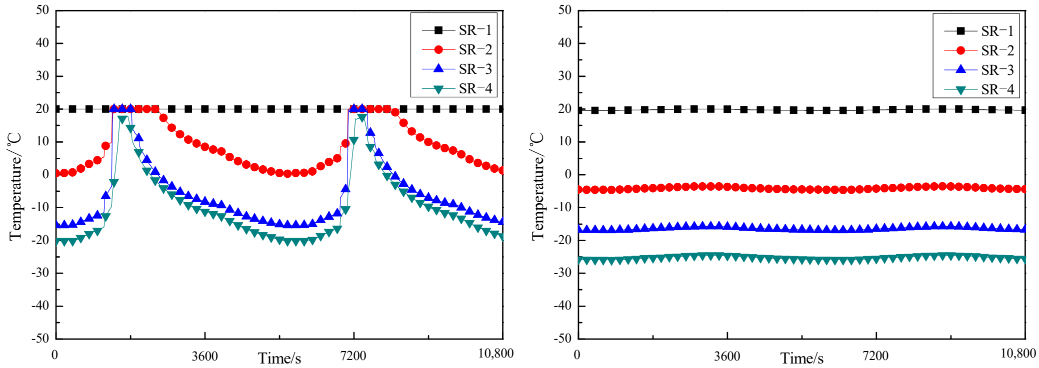

Figure 7. Temperature of the pipes on the secondary radiator vs. time diagram in simulation (**left**: hot case, **right**: cold case).

4. Thermal Management Verification

4.1. Ground Thermal Test

In order to verify that the thermal management meets the requirements of the remote sensor, a vacuum thermal test was performed in a huge space environment simulation vacuum chamber(VC), the inner wall of the VC was sprayed with black paint and cooled down to 100 K, the vacuum degree was about 1×10^{-5} Pa. Temperature measurement precision of the thermistor was about 0.1 °C. Temperature of satellite platform interface was the Dirichlet boundary condition, the external heat flux was the Neumann boundary condition, the heat sources generate heat according to the working mode. The external heat flux of the remote sensor entrance was simulated by an infrared heating cage, external heat flux of MLI and radiators was simulated by electric heaters. To eliminate the influence of gravity to LHP, the LHP and CCDs were at the same height, the capillary pump assembly was horizontal. When the test condition was met in VC, the transient external heat flux began to be simulated. Almost all the heaters started to work by temperature controller, except the heaters on evaporator and on preheater. The startup procedure of LHP was to set the heater on the preheater to work first, the temperature of the preheater changed from 22 °C to 29.6 °C, the liquid phase working medium turned to the gas phase, and the pressure generated pushed the working medium to the CC, so that the capillary wick in the CC was surrounded by more working medium; after that, we set the heater on the evaporator to work at 30 W, the temperature of the evaporator changed from 7.2 °C to 19.9 °C. The heated working medium vaporized and flowed along the gas phase pipe. At the same time, the capillary wick continuously replenished the working medium in the CC by capillary force, the temperature of the preheater and cold plates was about 20 °C, the LHP started up successfully, and after that, the heat power on the evaporator switched between 30 W and 90 W according to the working mode of CCD.

The temperature results of the main frame, lens structure, and mirrors are shown in Figure 8. It can be seen that the temperature fluctuation of the main frame, structure, and mirrors of lens were ±0.15 °C, ±0.1 °C, and ±0.05 °C, respectively.

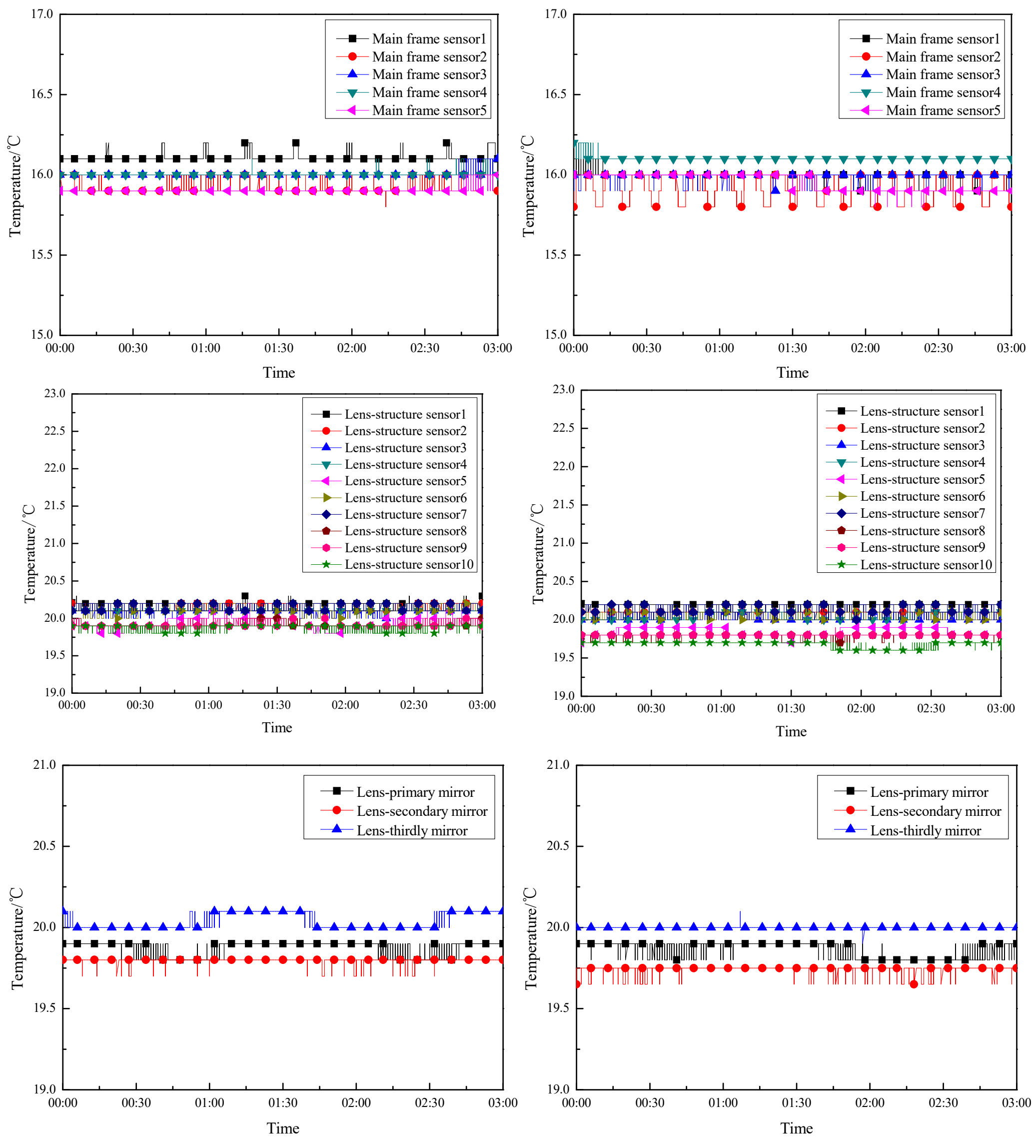

Figure 8. Temperature of the main frame and structure of lens vs. time diagram in test (**left**: hot case, **right**: cold case).

The period of orbit is about 95 min, the working time of CCD is 8 min every orbit in hot condition, and shutdown in cold condition. When the driving power switched from 30 W to 90 W 3 min before the CCDs working, the temperature of the evaporator increment was about 1 °C, the mass flow of LHP increased, a lot of sub-cooled working fluid flowed in to the CC and the pre-heater, the temperature of CC and pre-heater decreased, and the temperature of the cold plate dropped by about 0.5 °C. When the CCDs started working, the temperature of the CCD cold plates increased by about 1.1 °C. The temperature range of CCDs was 20.1 °C~21.7 °C in both cases, are shown in Figure 9.

In Figures 10 and 11 are the temperature of thermocouple positions along the pipe in the primary and secondary radiators. In the hot case, the length variation of the vapor–liquid phase zone is about 1.03 m and 0.97 m of the primary and secondary radiators, respectively. In the cold case, the vapor–liquid phase zone is stable, and agreed well with the numerical simulation.

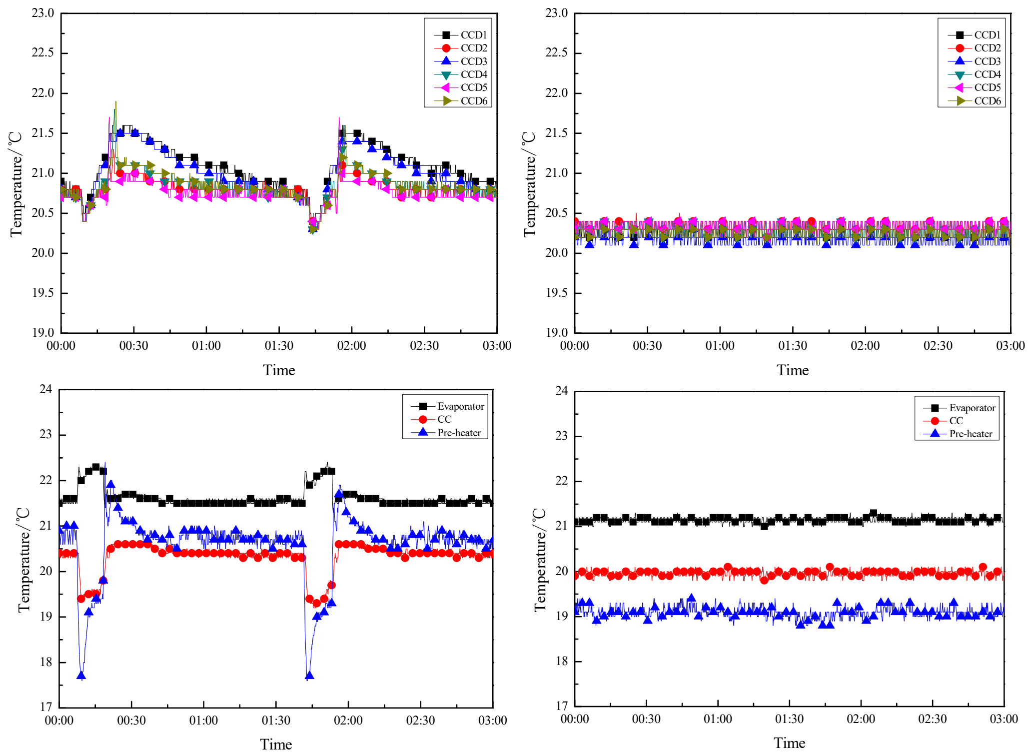

Figure 9. Temperature of the mirrors of lens and CCD cold plates vs. time diagram in test (**left**: hot case, **right**: cold case).

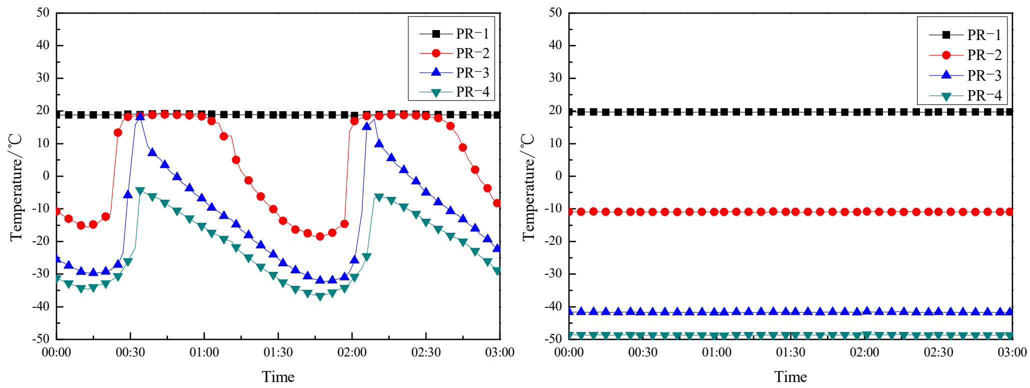

Figure 10. Temperature of the different position in primary radiator along the pipe vs. time diagram in test (**left**: hot case, **right**: cold case).

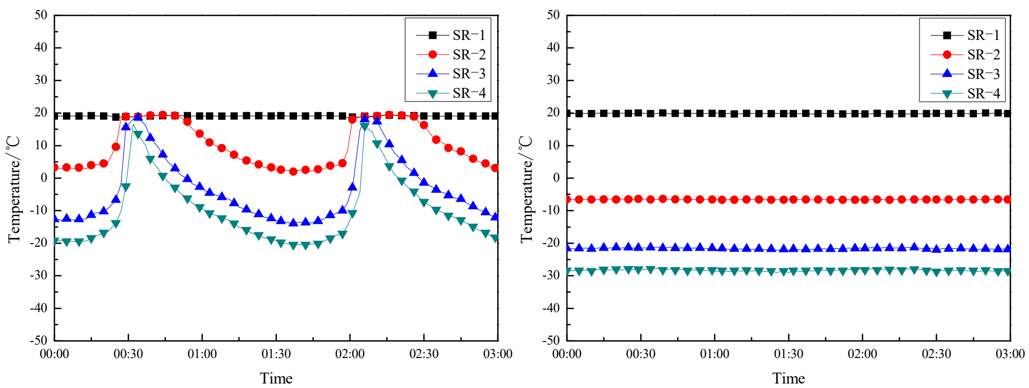

Figure 11. Temperature of the different position in secondary radiator along the pipe vs. time diagram in test (**left**: hot case, **right**: cold case).

4.2. On-Orbit Flying Validation

The temperature of the remote sensor on orbit over a year are shown in Figure 12. Temperature range of the main frame, structure of lens, primary mirror, CCDs are 15.9 °C~16.1 °C, 19.8 °C~20.2 °C,19.4 °C~19.7 °C, 19.6 °C~20.8 °C, respectively, and all of them meet the thermal control requirement.

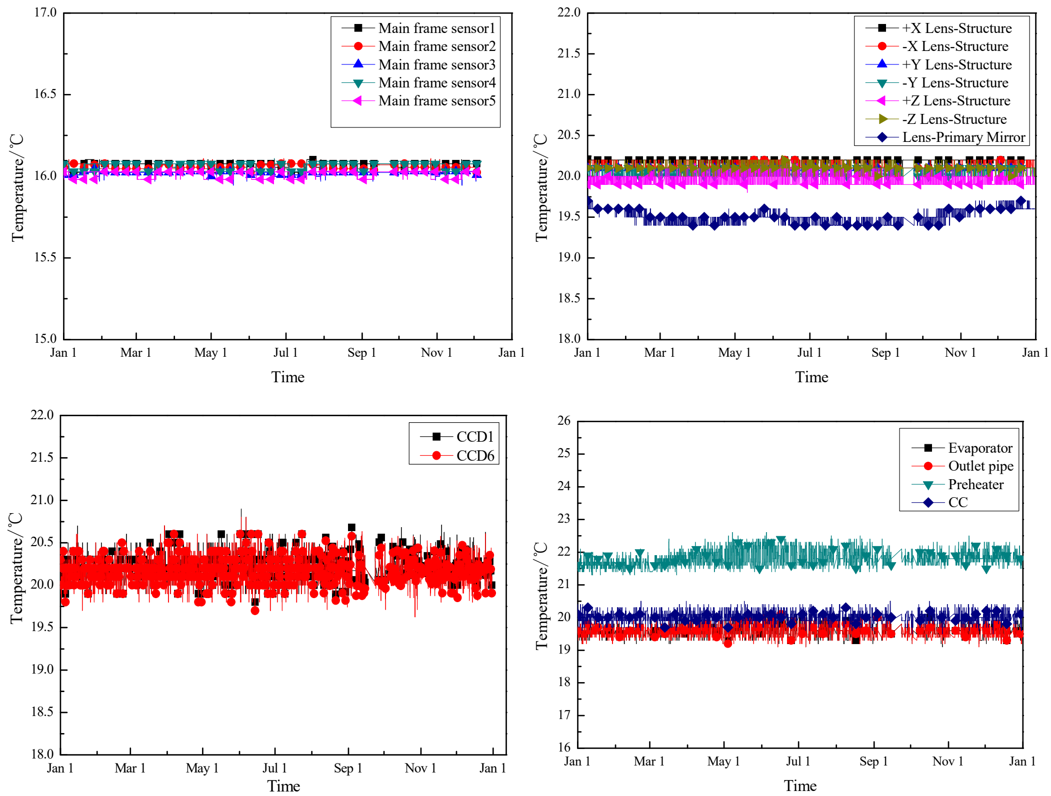

Figure 12. Temperature variation of different parts in remote sensor on-orbit.

5. Conclusions

According to the satellite power and thermal requirements of the remote sensor, an energy-saving thermal management system is presented, and a numerical simulation model is introduced. The results of the thermal test and the on-orbit temperature of key components show that:

1. For non-heat-source optical structure, three-stage external heat flux suppression technologies are suitable for large off-axis three-mirror reflection lenses, and the temperature fluctuation of the primary mirror is ±0.15 °C.
2. A low-energy-consumption loop heat pipe (LHP) was developed which can rapidly and automatically switch the driving power according to the working mode of the remote sensor. The averaged power consumption of the heater on evaporator is 37.57 W, and it saves 58.2% energy and mass compared to the conventional LHP, of which the heat power on evaporator is 90 W, the temperature variation of CCDs on-orbit is 19.6 °C~20.8 °C.
3. The dramatic change in CCDs' heat generation and driving power on evaporator result in vapor–liquid phase zone variation in two radiators. The result of the numerical simulation is about 1 m and 0.93 m of the primary and secondary radiators, respectively, and the result of the ground test is about 1.03 m and 0.97 m, respectively. The numerical simulation results agreed well with the experimental results.

Author Contributions: P.L.: Writing—original draft preparation; T.G.: methodology and resources; Q.C.: formal analysis; X.R.: writing—review and editing. All authors have read and agreed to the published version of the manuscript.

Funding: This research was funded by [National Key R&D Program of China] grant number [2021YFC2202102].

Data Availability Statement: Not applicable.

Conflicts of Interest: The authors declare no conflict of interest.

References

1. Cao, H.Y.; Liu, F.Q.; Zhao, C.G.; Dai, J. The study of high resolution stereo mapping satellite. *Natl. Remote Sens. Bull.* **2021**, *25*, 1400–1410.
2. Zhao, Z.; Meng, Q.; Zhang, H.; Zhao, H. Simulation and experimental study of mechanically pumped two-phase loop for CCD. *J. Beijing Univ. Aeronaut. Astronaut.* **2019**, *45*, 893–901.
3. Defisel, J.M. Lessons learned from the thermal design of an instrument (EIT, the Extreme-UV Imaging Telescope) onboard SOHO. In Proceedings of the 27th International Conference on Environmental Systems, University of Liège, Lake Tahoe, NV, USA, 14–17 July 1997; pp. 13–19.
4. Pranyies, P.; Deswarte, D.; Toubhans, I.; Le Goff, R. Sic focal plane assembly for the Pleiades HR Satellite. *Proc. SPIE-Int. Soc. Opt. Eng.* **2004**, *5570*, 568–576.
5. Li, S.; Chen, L.; Wu, Y. Thermal design of detector for the solar X-Ray and extreme ultraviolet imager. *J. Thermophys. Heat Transf.* **2019**, *33*, 285–291. [CrossRef]
6. Choi, M.K. *Thermal Design to Meet Stringent Temperature Gradient/Stability Requirements of SWIFT BAT Detectors*; AIAA-2000-2906[R]; AIAA: Washington, DC, USA, 2000; pp. 576–584.
7. Khrustalev, D.; Stouffer, C.; Ku, J.; Hamilton, J.; Andeson, M. Temperature control with two parallel small loop heat pipes for GLM program. *Front. Heat Pipes* **2015**, *5*, 9. [CrossRef]
8. Khrustalev, D.; Robertson, G.A. *Advances in Transient Modeling of Loop Heat Pipe Systems with Multiple Components*; AIP Publishing: Melville, NY, USA, 2010; pp. 55–67.
9. Hoff, C.J.; Rogers, P.D. Correlation of a Sinda /Fluid Model for a Switchbox Loop Heat Pipe. In Proceedings of the 34th National Heat Transfer Conference, Pittsburgh, PA, USA, 20–22 August 2000.
10. Yang, T.; Zhao, S.; Gao, T.; Zhao, Z.M.; Zhao, Y.; Li, C.L. Design and in-orbit application of temperature controlled loop heat pipe for aerospace distributed heat sources. *J. Astronaut.* **2021**, *42*, 798–806.
11. Gao, T.; Yang, T.; Zhao, S. Experimental research on temperature controlling performance of loop heat pipe in vacuum and low temperature environment. *Spacecr. Recovery Remote Sens.* **2019**, *40*, 38–47.
12. Cullimore, B.; Baumann, J. Steady state and transient loop heat pipe modeling. In Proceedings of the International Conference on Environmental Systems, Toulouse, France, 9–13 July 2000.
13. Ku, J. Operating characteristics of loop heat pipes. In Proceedings of the 29th International Conference on Environmental System, Denver, CO, USA, 12–15 July 1999; pp. 1–17.
14. Kaya, T.; Hoang, T.T. Mathematical modeling of loop heat pipes and experimental validation. *J. Thermophys. Heat Transf.* **1999**, *13*, 314–320. [CrossRef]
15. Pauken, M.; Rogriguez, J. *Performance Characterization and Model Verification of a Loop Heat Pipe*; SAE International: Warrendale, PA, USA, 2000.
16. Mahony, D.R.; Hoang, T.T.; Baldauff, R.W. *Model Simulation of a Two Loop Heat Pipe Thermal Control System in Low Earth Orbit*; SAE Technical Papers; SAE International: Warrendale, PA, USA, 2007.